Shape Sensitivity Analysis for Coupled Fluid-Solid Interaction Problems

Koorosh Gobal

August 24, 2016

Contents

List of Figures

List of Tables

Chapter 1

Shape Sensitivity Analysis for Coupled Fluid-Structure Interaction Problems

Fluid-Structure interaction (FSI) is a multiphysics coupling of the physical laws that govern fluid mechanics and structural dynamics. When the fluid flows over or inside a structure, it causes stresses on the solid object. These stresses can cause large or small deformations in the structure with leads to change in its shape. Depending on the magnitude of the stress, these deformations can be small or large. The effect of small deformations of the solid can be neglected since they do not affect the fluid flow. However, if the deformations are large, the pressure and velocity field of the fluid will change as a result.

In this chapter, we start with a survey of different coupling and solution methods available for solving a coupled FSI problem. To handle the mesh deformation shortcoming of large structural deformations, we will propose the IB method for managing these multiphysics simulations. We will build on the work of Chapter 4 to develop shape sensitivity analysis for a coupled FSI system. The shape sensitivity analysis developed here is demonstrated on various coupled systems. Throughout this chapter we consider the flow of *incompressible laminar Newtonian fluid* governed by Navier-Stokes (NS) equations interacting with an *elastic structure.*

1.1 Fluid-Structure Interaction

Considering fluidstructure interactions are vital in the design of numerous engineering systems such as aircraft and turbine blades especially in designs where fatigue is the dominant mode of failure. Neglecting the effects of oscillatory loads caused by fluid-structure interaction can yield to the catastrophic failure of designed systems. Tacoma Narrows Bridge (1940), is probably one of the most infamous examples of large-scale failure.

Computer simulations are often used to calculate the response of a system for a multiphysics and often nonlinear fluid-structure problem. There are two main approaches available for developing simulation tools for these coupled FSI problems [87]: 1) Partitioned approach and 2) Monolithic approach.

In a **partitioned** scheme, the fluid and the structure equations are alternatively integrated in time, and the interface conditions are enforced. Typically, partitioned methods are based on the following sequential process:

1. Transfer the location and velocity of the structure to the fluid domain.
2. Update the fluid mesh
3. Solve fluid's governing equation and calculate new pressure field
4. Apply pressure load on the structure
5. Advance the structural system in time under the fluid-induced load

This sequential process allows for software modularity. Partitioned schemes require only one fluid and structure solution per time step, which can be considered as a single fluidstructure iteration.

In the **monolithic** approach, the equations governing the flow and the displacement of the structure are solved simultaneously, with a single solver. The monolithic approach requires a code developed for this particular combination of physical problems whereas the partitioned approach preserves software modularity because an existing flow solver and structural solver are coupled. Moreover, the partitioned approach facilitates the solution of the flow equations and the structural equations with different, possibly more efficient techniques which have been developed specifically for either flow equations or structural equations. In this research, we are following the partitioned approach to the FSI problem. In this chapter we will couple the IB solver developed in Chapter 3 for solving the NS equations with an external finite element code to address the multiphysics problem.

The FSI solution procedure is also classified regarding the level of coupling between the two disciplines [88]. In the 1-way or weak coupling, the pressure loads are transferred to the structure, causing the solid domain to deform. However, the structural domain does not affect the fluid's mesh, and the solid domain deformations are not mapped back to the fluid domain. In this approach, each discipline is solved single time to calculate the response. On the other hand, in the 2-way or strong coupling, the solution of the coupled system is done in an iterative manner. The solution procedure starts with solving the fluid's governing equations. The pressure distribution at the fluid-structure boundary is then mapped to the solid domain to calculate the displacement of the structure. The deformation of the structure results in updating the fluid mesh. This is done until the solution is converged or the process is stopped manually. By using the IB method, mesh modification step of the strong coupling is removed in this work. As described in Chapter 3, by removing the mesh deformation step, we get a more robust simulation and decrease the computational expense of the coupled multiphysics analysis at the same time.

1.1.1 Governing Equations

The coupled motion of the fluid and solid domains is governed by a set of governing equations. The Navier-Stokes and continuity equations govern the fluids motion as shown in Equation (5.1) and the solid deformation is governed by a set of elastic equations as shown in Equation (5.2).

$$\rho^f \frac{\partial \mathbf{u}^f}{\partial t} + \rho^f \mathbf{u}^f \cdot \nabla \mathbf{u}^f = \nabla \cdot \sigma^f + \rho^f \mathbf{f}^f \qquad : \text{Conservation of momentum} \tag{1.1a}$$

$$\nabla \cdot \mathbf{u}^f = 0 \qquad : \text{Conservation of mass} \tag{1.1b}$$

$$\sigma^f = \mu \left[\nabla \mathbf{u}^f + \left(\nabla \mathbf{u}^f \right)^T \right] - p^f \mathbf{I} \qquad : \text{Stress formula} \tag{1.1c}$$

$$\rho^s \dot{\mathbf{u}}^s = \nabla \cdot \sigma^s + \mathbf{f}^s \qquad : \text{Equation of motion} \tag{1.2a}$$

$$\epsilon^{\mathbf{s}} = \frac{1}{2} \left[\nabla \mathbf{d}^s + (\nabla \mathbf{d}^s)^T \right] \qquad : \text{Strain-displacement equation} \tag{1.2b}$$

$$\sigma^s = \mathbf{C} : \epsilon^s \qquad : \text{Constitutive equation} \tag{1.2c}$$

In the above equations, superscript 'f' and 's' correspond to the fluid and solid properties respectively. In Equation (5.1) ρ^f, $\mathbf{u}^f$, p^f, and $\mathbf{f}^f$ correspond to the fluid density, velocity, pressure, and body forces respectively. It should be noted that the immersed boundary forces are applied through the body force term $\mathbf{f}^f$. In Equation (5.2) ρ^s, $\mathbf{u}^s$, $\mathbf{f}^s$, $\mathbf{d}^s$, and C correspond to the solid density, velocity, body force, displacement, and stiffness tensor. We chose d to represent the displacement so that it won't be confused with the velocity term u. This is required when we are defining the IB conditions over the boundary. It should be noted that $\mathbf{C} : \epsilon^s$ defined the inner product of two second order tensors and is equation to $\mathbf{C}_{ij}\epsilon^s_{ij}$. In this chapter, we assume that the body force term in the solid's equation, $\mathbf{f}^s$, is equal to zero. The fluid's body force term is calculated based on the virtual boundary method as described in Chapter 3.

In order to couple the fluid and solid equations of (5.1) and (5.2), we are imposing a set of kinematic and dynamic constraints [89] at the intersection of the two mediums as defined in Equation (5.3).

$$\mathbf{u}^s - \mathbf{u}^f = 0 \qquad : \text{Kinematic constraint} \tag{1.3a}$$

$$\sigma^s \cdot \mathbf{n} - \sigma^f \cdot \mathbf{n} = 0 \qquad : \text{Dynamic constraint} \tag{1.3b}$$

The kinematic constraint will result in zero relative velocity between the fluid and solid domains whereas the dynamic constraint will lead to the transfer of loads between the two physical mediums.

1.1.2 Multidisciplinary Coupling

In Chapter 3, we utilized the Regularized Delta (RD) function to transfer the velocity information from the Eulerian nodes to the Lagrangian nodes to calculate the force terms needed for the IB method. The same idea is used here to calculated the pressure loads acting on the solid domain. As shown in Figure 5.1, by solving the NS equations, the magnitude of the pressure field at each fluid (Eulerian) node (x_i) is known.

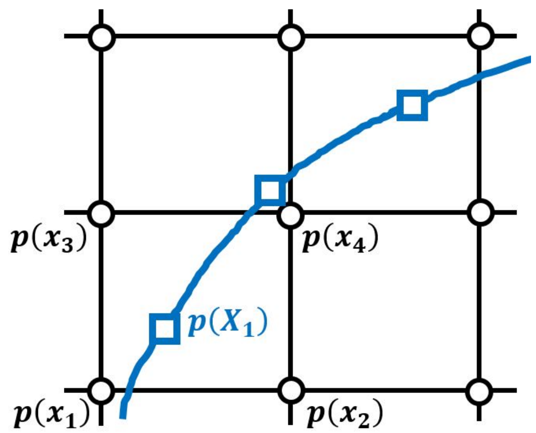

Figure 1.1: Eulerian (◯) and Lagrangian (□) nodes for pressure values near and on the immersed boundary.

To map this pressure information from the Eulerian nodes, x_i, to the Lagrangian node, X, we convolute the pressure field calculated from the CFD simulation with RD function of Equation (5.4a). By this approach, we have calculated the pressure load on the structure. This is shown in Equation (5.4b)

$$\mathcal{D}(x, X) = \frac{-\tanh^2\left(\dfrac{x-X}{\eta}\right)+1}{2\eta} \tag{1.4a}$$

$$p(X, Y) = \int\int p(x, y)\mathcal{D}(x, X)\mathcal{D}(y, Y)dxdy \tag{1.4b}$$

By applying this pressure distribution on the solid domain and solving the equation of motion, we can calculate the displacement and the resulting velocity of the solid structure. The structure new location is used to update the RD function used for data transfer between the Eulerian and Lagrangian nodes. The cost of updating the RD functions for IB method is minuscule compared to the effort required to update the mesh in body conformal discretization approaches. The velocity of the solid domain is used for calculating the force terms required by the IB method as shown in Equation (5.5).

$$\mathbf{f}(\mathbf{X},t) = \alpha \int_0^t \left[\mathbf{u}(\mathbf{X},\tau) - \mathbf{V}(\mathbf{X},\tau)\right] d\tau + \beta \left[\mathbf{u}(\mathbf{X},\tau) - \mathbf{V}(\mathbf{X},\tau)\right] \tag{1.5}$$

As described in Chapter 4, $\mathbf{u}(\mathbf{X},\tau)$, is the velocity of fluid calculated at the Lagrangian point $\mathbf{X}$ at time τ, and $\mathbf{V}(\mathbf{X},\tau)$ is the velocity of the solid structure at the same location and time. The later is calculated after solving the structure's equation of motion. This loop is continued until the convergence is meet or the process stoped manually. The flowchart for the fluid-solid interaction using the IB method is shown in Figure 5.2.

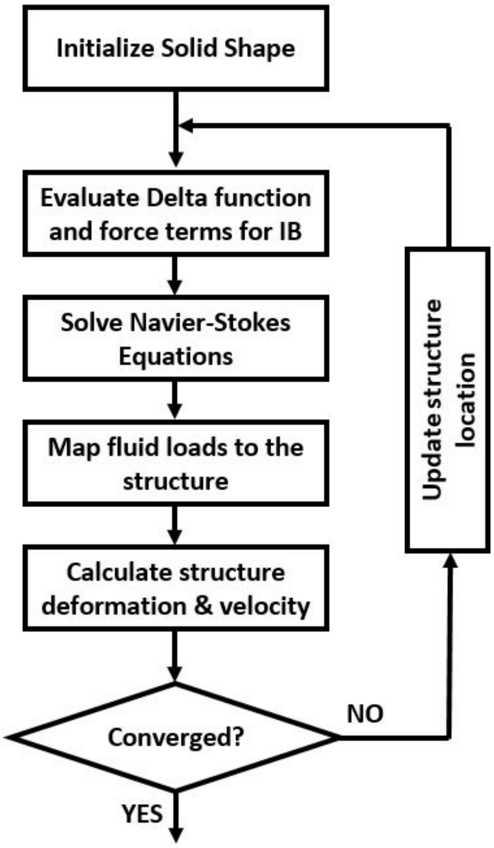

Figure 1.2: Fluid-solid interaction analysis using IB method flow chart.

1.2 Multidisciplinary shape sensitivity analysis

The shape sensitivity analysis for the coupled multidisciplinary problem is built on the work done in Chapter 4. However, in this chapter we are also including the shape sensitivity effects on the structural side. To do so, we differentiate Equations (5.1) and (5.2) alongside the kinematic and dynamic constraints of Equation (5.3) with respect to shape design variable, b. The sensitivity equations for the fluid and solid domains are shown in Equation (5.6) and (5.7) respectively.

$$\rho^f \frac{\partial}{\partial t}\left(\frac{\partial \mathbf{u}^f}{\partial b}\right) + \rho^f \frac{\partial \mathbf{u}^f}{\partial b} \cdot \nabla \mathbf{u}^f + \rho^f \mathbf{u}^f \cdot \nabla \left(\frac{\partial \mathbf{u}^f}{\partial b}\right) = \nabla \cdot \left(\frac{\partial \sigma^f}{\partial b}\right) + \rho^f \frac{\partial \mathbf{f}^f}{\partial b} \quad (1.6a)$$

$$\nabla \cdot \left(\frac{\partial \mathbf{u}^f}{\partial b}\right) = 0 \quad (1.6b)$$

$$\frac{\partial \sigma^f}{\partial b} = \mu \left[\nabla \left(\frac{\partial \mathbf{u}^f}{\partial b}\right) + \nabla \left(\frac{\partial \mathbf{u}^f}{\partial b}\right)^T\right] - \frac{\partial p^f}{\partial b}\mathbf{I} \quad (1.6c)$$

$$\rho^s \frac{\partial \dot{\mathbf{u}}^s}{\partial b} = \nabla \cdot \left(\frac{\partial \sigma^s}{\partial b} \right) + \frac{\partial \mathbf{f}^s}{\partial b} \tag{1.7a}$$

$$\frac{\partial \epsilon^{\mathbf{s}}}{\partial b} = \frac{1}{2} \left[\nabla \frac{\partial \mathbf{d}^s}{\partial b} + \nabla \left(\frac{\partial \mathbf{d}^s}{\partial b} \right)^T \right] \tag{1.7b}$$

$$\frac{\partial \sigma^s}{\partial b} = \frac{\partial \mathbf{C}}{\partial b} : \epsilon^s + \mathbf{C} : \frac{\partial \epsilon^s}{\partial b} \tag{1.7c}$$

$$\frac{\partial \mathbf{u}^s}{\partial b} - \frac{\partial \mathbf{u}^f}{\partial b} = 0 \tag{1.8a}$$

$$\frac{\partial \sigma^s}{\partial b} \cdot \mathbf{n} - \frac{\partial \sigma^f}{\partial b} \cdot \mathbf{n} = 0 \tag{1.8b}$$

As shown in Equations (5.6) and (5.7), to solve the sensitivity equations we need to have the solution of the governing equation ($\mathbf{u}^f$, $\epsilon^{\mathbf{s}}$). Therefore, we are proposing to use the flowchart of Figure 5.3 for the coupled multidisciplinary sensitivity analysis. The sensitivity calculation process starts by solving the Navier-Stokes equation and mapping the pressure to the structural domain to calculate the deformation in the structural domain. The solution of the Navier-Stokes and Elasticity equations are then fed to the sensitivity solver to calculate the sensitivity response. This loop is continued until a convergence for the governing equations is reached, or the process is stopped manually.

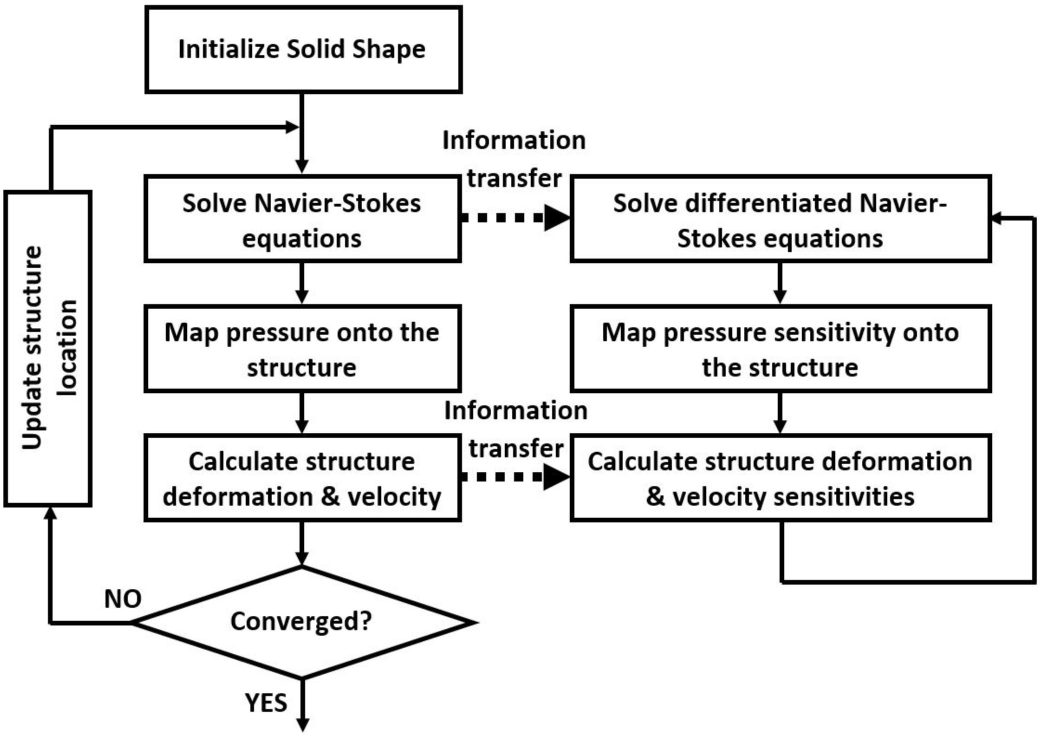

Figure 1.3: Coupled multidisciplinary sensitivity analysis flowchart.

1.3 Demonstration Problems

1.3.1 Vortex induced vibration

Vortex induced vibrations (VIV) are motions of solid structures immersed in fluid that is caused by the irregularities in the flow. VIV of structures is of practical interest to many fields of engineering. For example, it can cause vibration and noise in heat exchanger tubes and aircraft wing. The practical significance of VIV has led to various studies that are discussed in the literature[90]. In this demonstration problem, we are interested in the forced oscillations of an elastically mounted rigid cylinder for different values of the Reynolds number. The physical problem is shown in Figure 5.4.

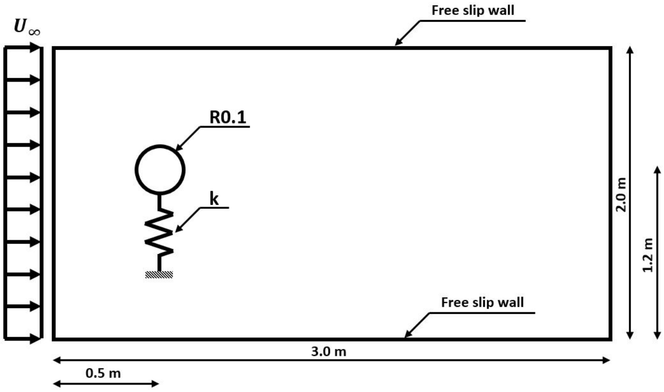

Figure 1.4: Physical domain for the vortex induced vibration problem.

The rigid cylinder has the radius of R and mounted on an elastic structure with stiffness k. The free steam velocity is selected as U_∞. To verify the solver and FSI coupling, we are going to calculate the shedding frequency of the cylinder first. Vortex shedding is an oscillating flow that takes place when fluid passes a bluff body at certain velocities. The vortices that are generated on the aft of the body start to detach periodically from either side of the body. The frequency at which the vortex shedding takes place is described using the dimensionless Strouhal number. The Strouhal number is defined as shown in Equation (5.9).

$$St = \frac{fL}{U} \tag{1.9}$$

where f is the frequency of the vortex shedding, L is the characteristic length, and U is the flow velocity. The Strouhal number of a stationary circular cylinder is a function of Reynolds number [91] as shown in Figure 5.5[1].

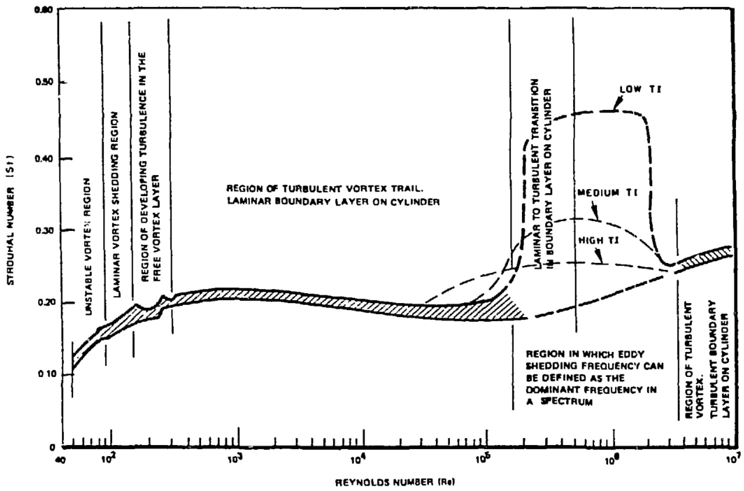

Figure 1.5: Strouhal number for a single cylinder [1].

To verify the simulation code developed for the IB simulation, we verified the shedding frequency of the circular cylinder in the cross-flow. The domain length and height are selected as $3m$ and $2m$ respectively as shown in Figure 5.4. The cylinder radius is selected as $0.1m$ and is located $0.5m$ from the left wall and $1.2m$ from the bottom wall. The asymmetric shape of the computational domain helps the shedding initiation. The domain is discretized using 3000 cells in the x and 2000 in the y direction. The cylinder is defined using 50 Lagrangian nodes. The p value in the delta function definition is selected as 0.5. It should be noted that to verify the shedding frequency the cylinder is fixed in its place. We compared the Strouhal number calculated from the IB code with the results [92] for two different Reynolds numbers. The shedding frequency is calculated by saving the time history of drag force on the cylinder and performing frequency analysis on this data. We used the power spectral density function to look at the most dominant frequencies. The comparison between these results is shown in Table 5.1.

Reynolds number	St (current IB)	St (Literature [1] and [92])
100	0.171	0.168
500	0.194	0.200

Table 1.1: Comparison between the shedding frequency calcualted using IB method and results from the literature.

The effect of number of Lagrangian points on the shedding frequency is shown in Figure 5.6 for the two Reynolds numbers of 100 and 500. As shown here, number of Lagrangian points does not affect the vortex shedding frequency.

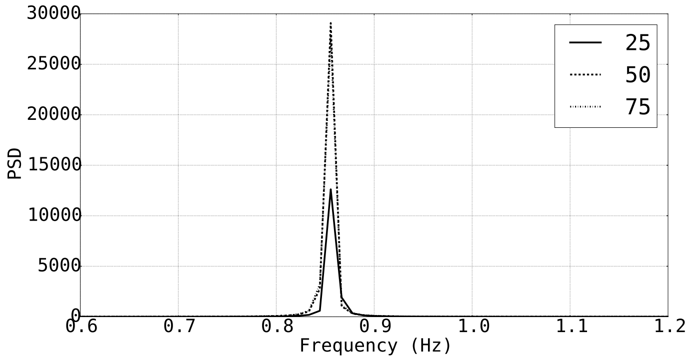

(a) $Re = 100$

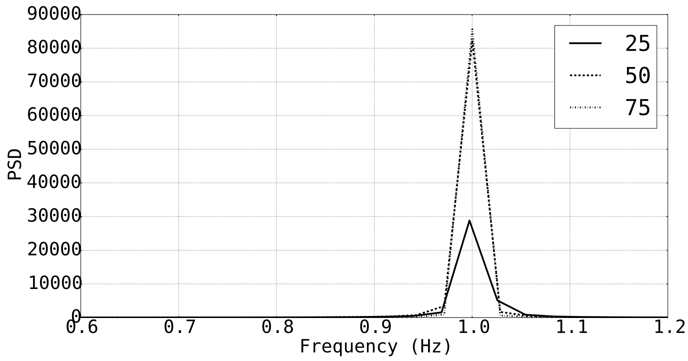

(b) $Re = 500$

Figure 1.6: Number of Lagrangian points effect on the shedding frequency.

After verifying the shedding frequency of IB solver, we attach the elastic structure to the cylinder and let the system vibrate due to the aerodynamic loads. The equation of motion for this cylinder is shown in Equation (5.10).

$$m\ddot{y} + ky = f(y, \dot{y}, t; R) \tag{1.10}$$

where y is the cylinder location, m is the cylinder mass, k is elastic structure stiffness, and $f(y, \dot{y}, t; R)$ is the aerodynamic load. It should be noted that the load is an explicit function of cylinder location, velocity, time, and an implicit function of cylinder radius. This requires an unsteady treatment of the FSI problem by coupling Equation (5.1) and (5.10).

At each time step, the NS equations are solved and the pressure values at the Lagrangian nodes are calculated using the regularized Delta function. These pressure values are then integrated over the cylinder surface to calculate the force value on the right-hand-side of Equation (5.10). To solve for the structure displacement and velocity, Equation (5.10) is written in the state-space form as shown in Equation (5.11). This equation is then integrated in time alongside the NS equations using Adams-bashforth method. The initial condition for the structure is selected as zero displacement and velocity at $t = 0$.

$$\begin{bmatrix} \dot{y} \\ \ddot{y} \end{bmatrix} = \begin{bmatrix} 0 & 1 \\ -\dfrac{k}{m} & 0 \end{bmatrix} \begin{bmatrix} y \\ \dot{y} \end{bmatrix} + \begin{bmatrix} 0 \\ f(y, \dot{y}, t; R) \end{bmatrix} \tag{1.11}$$

where the load, $f(y, \dot{y}, t; R)$, is calculated as shown in Equation (5.12).

$$f = \oint \left(\int \int p(x, y)\mathcal{D}(x - X_s)\mathcal{D}(y - Y_s)dxdy \right) ds \tag{1.12}$$

In Equation (5.12), $p(x, y)$ is the pressure calculated from the CFD solution, $\mathcal{D}$ is the regularized delta function, and ds represents the infinitesimal element on the cylinder surface.

For the coupled FSI sensitivity analysis we looked at the vortex induced vibration of the cylinder at two different Reynolds numbers. The sensitivity of the displacement to the radius of the cylinder is calculated and verified with the complex step results. The sensitivity equations for the fluid domain is derived in Chapter 4 and by solving it we have the sensitivity of pressure field on the surface of the cylinder. The sensitivity equation for the structure is derived by differentiating Equation (5.11) as shown in Equation (5.13).

$$\begin{bmatrix} \dot{y'} \\ \ddot{y'} \end{bmatrix} = \begin{bmatrix} 0 & 1 \\ -\dfrac{k}{m} & 0 \end{bmatrix} \begin{bmatrix} y' \\ \dot{y'} \end{bmatrix} + \begin{bmatrix} 0 \\ f'(y, \dot{y}, t; R) \end{bmatrix} \tag{1.13}$$

here, $()'$, represents the derivative with respect to the design variable. As can be seen here, the same solver used for solving Equation (5.11) is utilized for solving Equation (5.13). The only difference between the two is the loads used for evaluating the right-hand-side of Equation (5.13).

For this problem the stiffness of the elastic structure, k, is selected as 1 N/m and the cylinder mass is chosen as 1 kg. The time history of cylinder displacement in the first 25 seconds of its motion is shown in Figure 5.7. As can be seen here, the cylinder starts from the initial position at $y = 1.2$ and after a short transient region starts oscillating at an almost constant amplitude. As shown in Figure 5.7

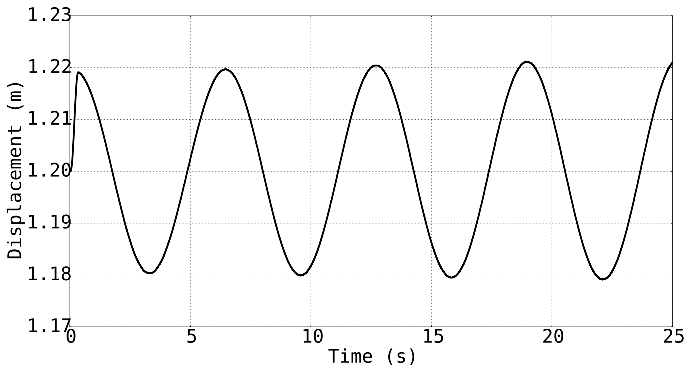

(a) $Re = 100$

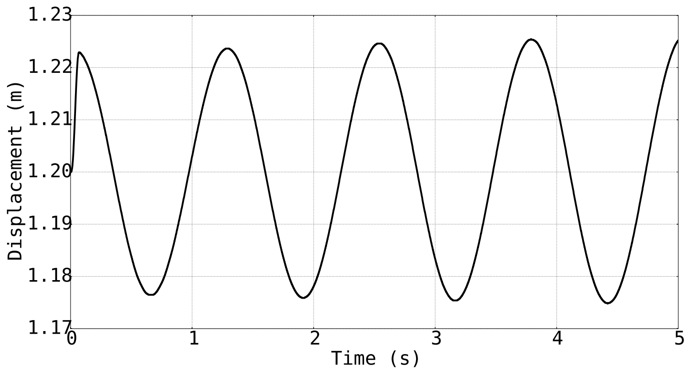

(b) $Re = 500$

Figure 1.7: Time history of cylinder center displacement.

Figure 5.8 shows the u-velocity contour around the elastically mounted cylinder at different times. As can be seen, the vortex shedding is dominant at $t = 5$. It should be noted that the vortex shedding starts before $t = 5$ and causes the cylinder to oscillate.

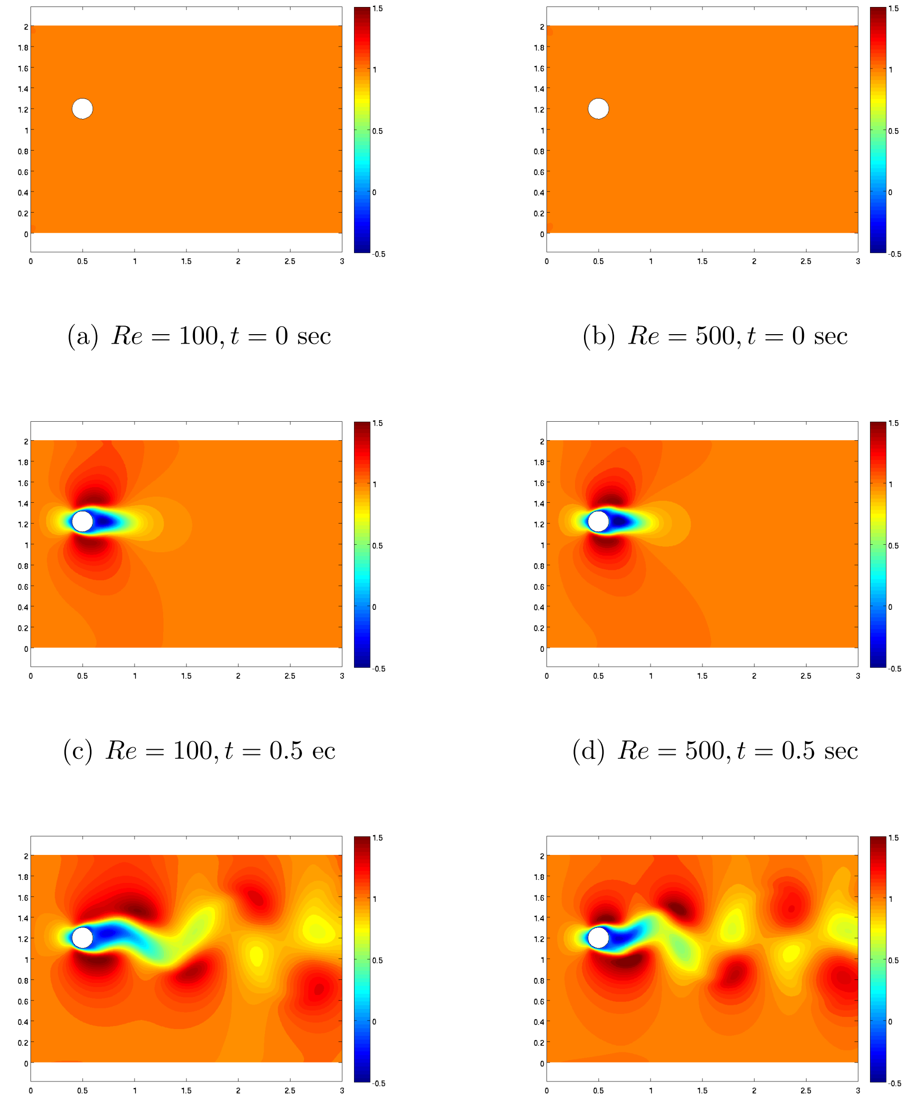

(a) $Re = 100, t = 0$ sec

(b) $Re = 500, t = 0$ sec

(c) $Re = 100, t = 0.5$ ec

(d) $Re = 500, t = 0.5$ sec

(e) $Re = 100, t = 5$ sec

(f) $Re = 500, t = 5$ sec

Figure 1.8: Unsteady u-velocity contours for flow around cylinder at $Re = 100$ and $Re = 500$.

The time history of the sensitivity results are shown and verified with the complex step solution in Figure 5.9. As shown here, As the initial time the sensitivity of displacement with respect to radius is zero since the cylinder is not moving. However, the value of cylinder displacement will start oscillating between positive and negative numbers as the simulation continuous. This is what we are expecting since by increasing the radius, the loads on the cylinder will increase. This will result in increase in the amplitude in both ends of the oscillation period.

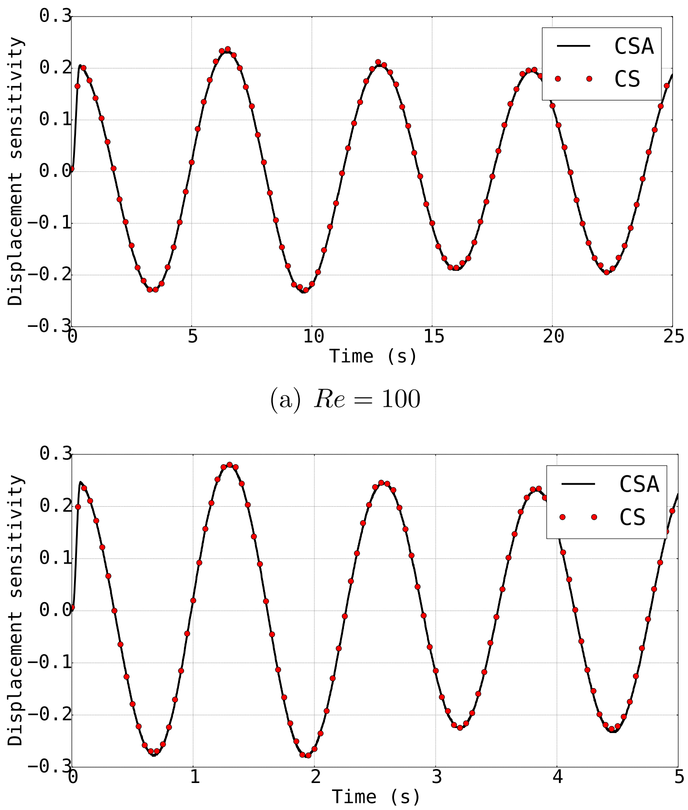

(a) $Re = 100$

(b) $Re = 500$

Figure 1.9: Time history of cylinder center displacement sensitivity.

Figure 5.10 shows the u-velocity sensitivity contour around the elastically mounted cylinder at different times. As shown in the sensitivity contours, the change in the cylinder radius mainly affects the downstream flow. This is expected for a convective flow where the information from cylinder cannot move upstream. The small region with negative sensitivity near the surface is due to the reduction of velocity due to boundary layer expansion as the radius increases and has physical meaning.

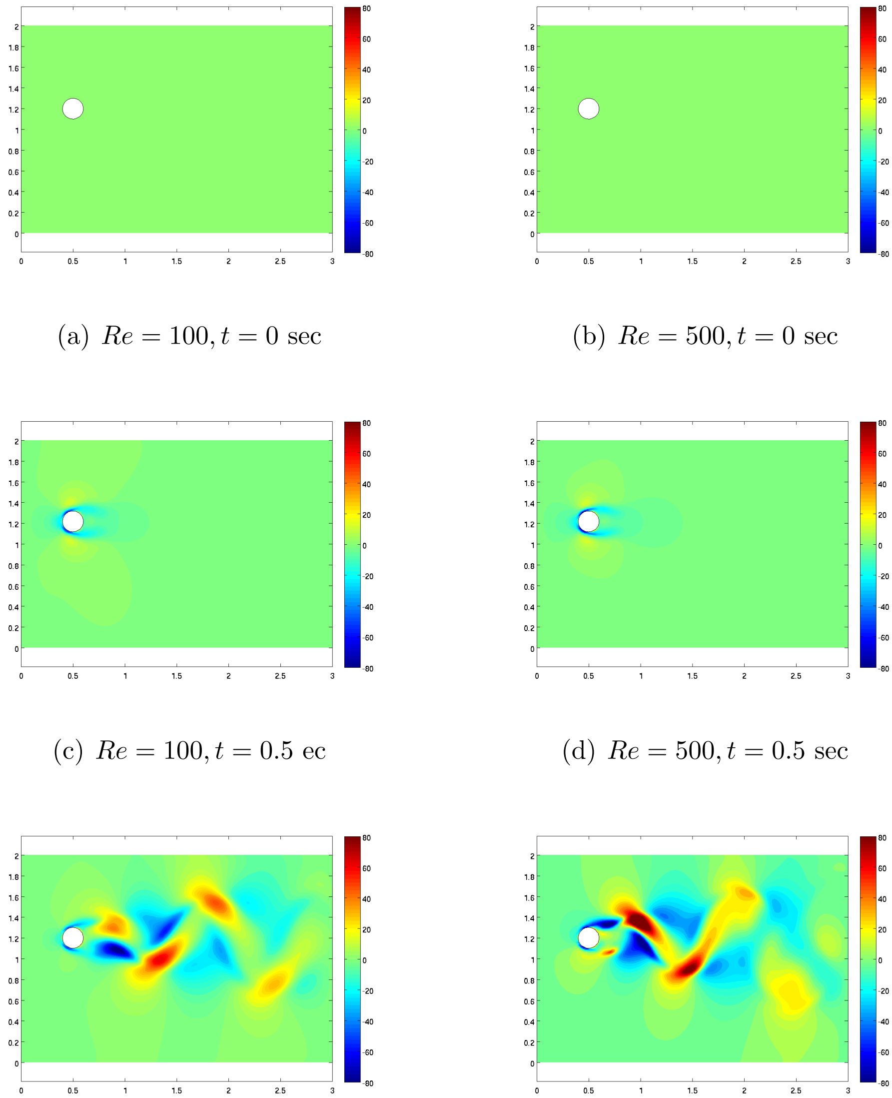

(a) $Re = 100, t = 0$ sec

(b) $Re = 500, t = 0$ sec

(c) $Re = 100, t = 0.5$ ec

(d) $Re = 500, t = 0.5$ sec

(e) $Re = 100, t = 5$ sec

(f) $Re = 500, t = 5$ sec

Figure 1.10: Unsteady u-velocity contours for flow around cylinder at $Re = 100$ and $Re = 500$.

1.3.2 Pitch and plunge airfoil motion

Understanding the unsteady aerodynamics characteristics of a pitching and plunging airfoil has two major engineering applications. First, it can be used to predict the dynamic stall of aerodynamic bodies such as aircraft in a demanding maneuver [93]. Dynamic stall is often seen in aerodynamic surfaces going through a pitching moment or oscillatory behavior. This phenomenon is caused due to instability and separation of the leading-edge vortex which results in a dramatic decrease in lift and sudden increase in pitching moment. Dynamic stall can lead to high amplitude vibrations and high loads that can cause fatigue and structural failure of the aerodynamic surfaces. The other motivation of investigating this unsteady aerodynamic behavior is the application of flapping wings for swimming and flying animals [94]. The vast majority of research on the pitching and plunging airfoil is done by forcing the motion on the airfoil and looking at the aerodynamic response. This is mainly done for investigating the thrust and the parameters that control it [95, 96]. Webb, et al. investigated the use of Immersed Boundary method for the forced pitching and plunging movement of the SD7003 airfoil and verified their solution with experimental results [97]. In this work, we are interested in the free oscillations of the airfoil due to aerodynamic loads. Moreover, we will investigate the sensitivity of the airfoil displacement to its shape.

To have an analytical representation of the airfoil shape, we used the Joukowsky transform to define the geometry. Joukowsky transform is a conformal mapping that maps a circle in the complex plane to a shape that represents a typical airfoil shape. The Joukowsky transform is shown in Equation (5.14).

$$z = \zeta + \frac{1}{\zeta} \quad , \quad \zeta = x + iy \tag{1.14}$$

As shown in Figure 5.11, the center location of the original circle defines the thickness and camber of the airfoil. For the sensitivity analysis, we are interested in the sensitivity of flow to the chamber; therefore, it is required to differentiated to the y coordinate of circle center. This is calculated analytically.

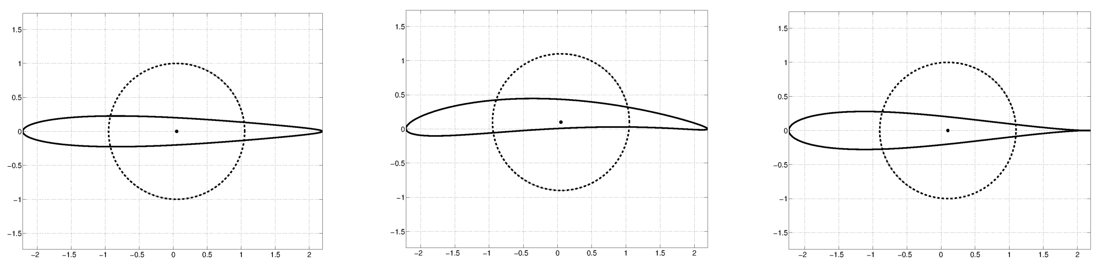

(a) $x_c = 0.05, y_c = 0.0$ (b) $x_c = 0.05, y_c = 0.1$ (c) $x_c = 0.1, y_c = 0.0$

Figure 1.11: Effect of circle location on Joukowsky airfoil shape.

The computational domain for this problem is defined as shown in Figure 5.12(a). The rigid airfoil is mounted on a two degree-of-freedom elastic structure as shown in Figure 5.12(b). The elastic structure contains an axial and torsional spring to represent better and actual wing.

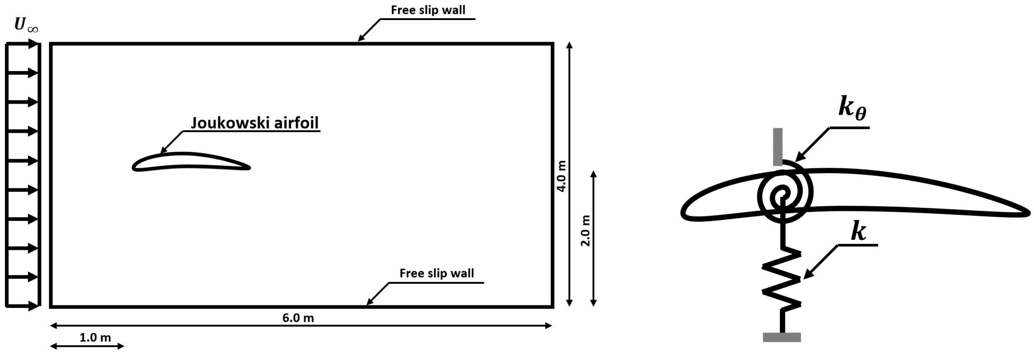

(a) Physical domain. (b) Airfoil elastic structure

Figure 1.12: Physical domain and elastic structure for the pitching and plunging airfoil.

The governing equations for the elastic structure in the state-space form are shown in Equation (5.15).

$$\begin{bmatrix} \dot{y} \\ \ddot{y} \\ \dot{\theta} \\ \ddot{\theta} \end{bmatrix} = \begin{bmatrix} 0 & 1 & 0 & 0 \\ -\dfrac{k}{m} & 0 & 0 & 0 \\ 0 & 0 & 0 & 1 \\ 0 & 0 & -\dfrac{k_\theta}{I} & 0 \end{bmatrix} \begin{bmatrix} y \\ \dot{y} \\ \theta \\ \dot{\theta} \end{bmatrix} + \begin{bmatrix} 0 \\ F\left(y, \dot{y}, t\right) \\ 0 \\ M\left(\theta, \dot{\theta}, t\right) \end{bmatrix} \tag{1.15}$$

where m is airfoil mass, k is axial spring stiffness, I is airfoil moment of inertia around its quarter-chord, k_θ is rotational spring stiffness, F is the force in y direction (lift generated by airfoil), and M is the moment at quarter-chord. The force and moment are calculated using the pressure field from the solution of NS equations. Adams-bashforth method is used to explicitly integrate Equation (5.15) in time.

For this problem we look at two different airfoils mounted on the elastic structure as shown in Figure 5.13. The difference in airfoil shape will result in different characteristics in the FSI response of the system. From now we refer to the airfoil defined in Figure 5.13(a) as *thin airfoil* and the one in Figure 5.13(b) as *thick airfoil*.

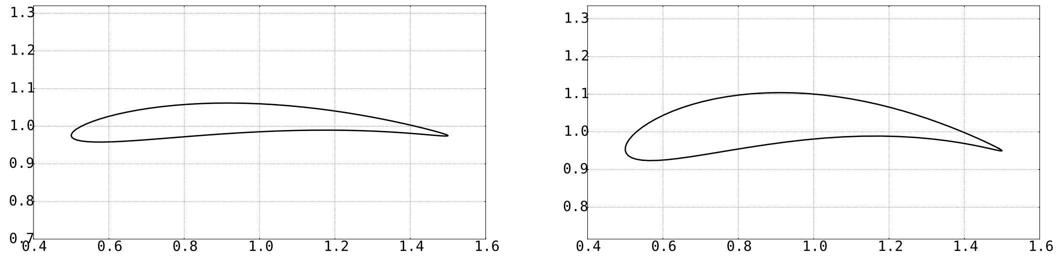

(a) $x_c = 0.05, y_c = 0.1$ (b) $x_c = 0.1, y_c = 0.2$

Figure 1.13: Airfoil shape used for FSI calculation.

The Reynolds number for this simulation is selected as 100. Higher Reynolds number will result in turbulent flow which is not considered in this research, and therefore the solution results for higher Reynolds numbers does not represent a physical solution. For the elastic structure properties, spring stiffness is selected as $0.5N/m$, airfoil mass as $1.0Kg$, rotational spring as $0.1N/\theta$, and the moment of inertia as $1.0Kg \cdot m^2$. The results of the first 50-second simulation of the airfoil center location and change in the angle of attack due to aerodynamic loads are shown in Figure 5.14. As shown here, the thin airfoil of Figure 5.13(a) follows an oscillatory response whereas the thick airfoil of Figure 5.13(b) experience divergence.

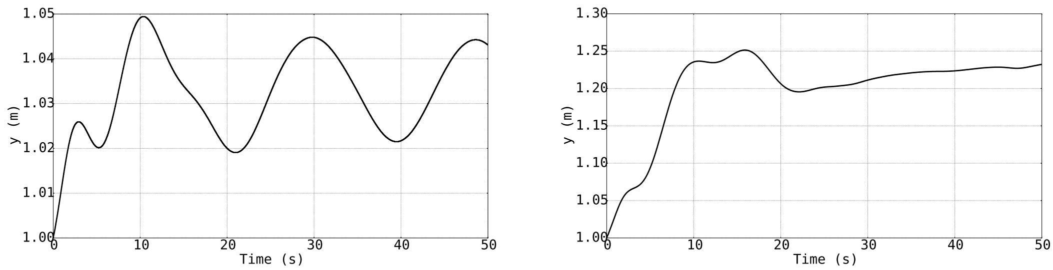

(a) Thin airfoil displacement (b) Thick airfoil displacement

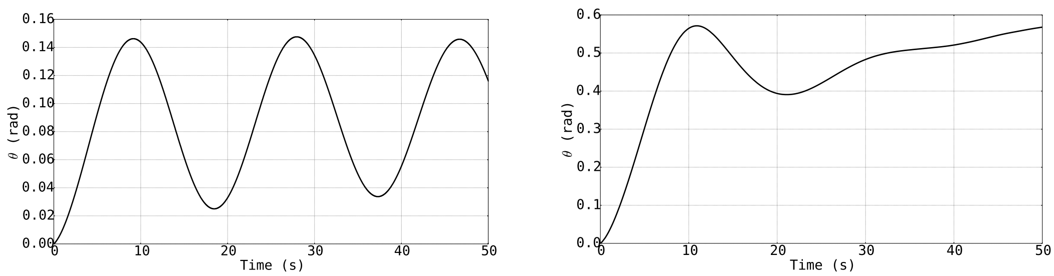

(c) Thin airfoil rotation (d) Thick airfoil rotation

Figure 1.14: Airfoil displacement and rotation results due to aerodynamic loads.

To better understand the solution history, three snapshots from the u-velocity contour of the two airfoils are shown in Figure 5.15. As shown here, the thick airfoil goes through large displacement and deformation. This is difficult to capture using the conventional body-conformal method; however, can be done with rather ease by utilizing the current IB approach.

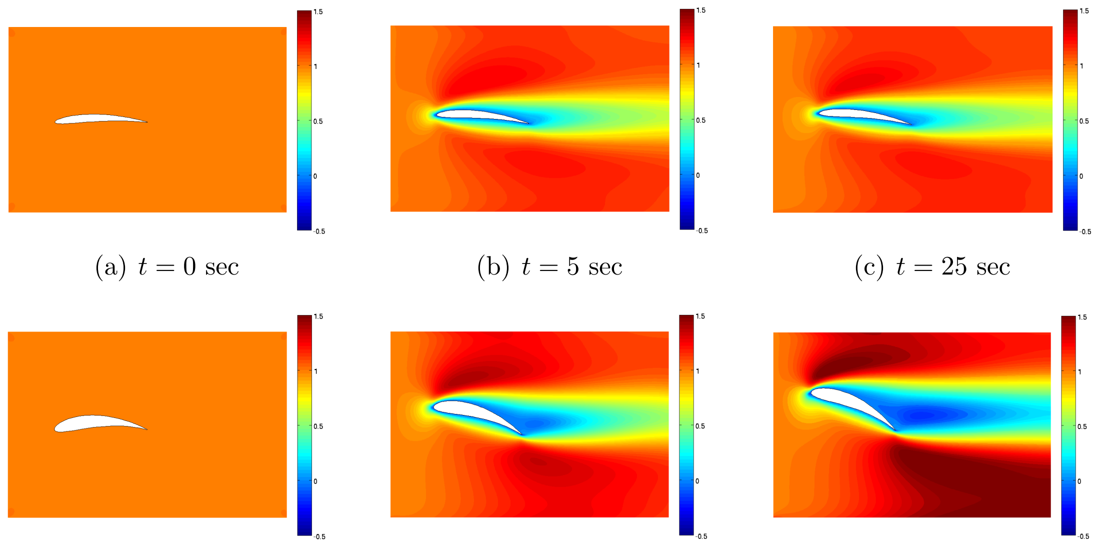

(a) $t = 0$ sec (b) $t = 5$ sec (c) $t = 25$ sec

(d) $t = 0$ sec (e) $t = 5$ sec (f) $t = 25$ sec

Figure 1.15: U-velocity time snapeshots for airfoil on elastic structure.

For the sensitivity analysis, we investigate the sensitivity of the airfoil displacement and rotation to change in its chamber. As discussed in Chapter 4, as a part of sensitivity calculation, it is required to derive the shape sensitivities. This is done analytically since the Joukowski transform provides us with an analytical definition for the airfoil boundary. The shape sensitivity of the airfoil to camber is calculated by differentiating Equation (5.14) to the y coordinate of the center of the airfoil. For the structure side, the shape only affects the loads acting on the elastic structure and not its shape. Therefore, we can use the same solver used for calculating the displacement and rotation of the structure for the sensitivity calculation. The time history of the sensitivity results for the displacement and rotation of the two airfoils is shown in Figure 5.16.

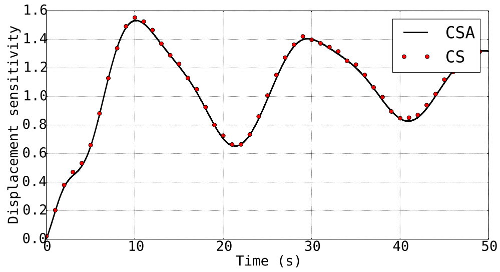

(a) Thin airfoil displacement sensitivity

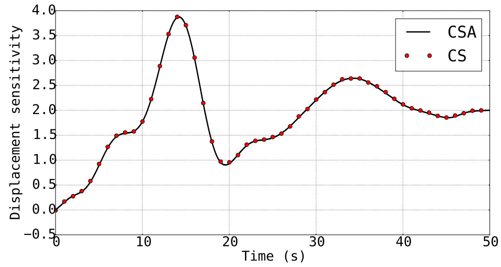

(b) Thick airfoil displacement sensitivity

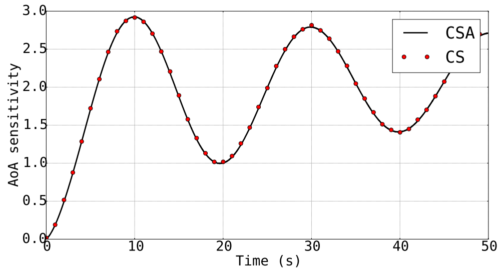

(c) Thin airfoil rotation sensitivity

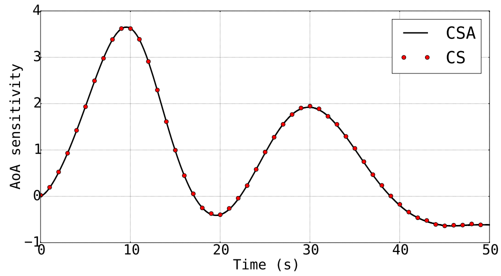

(d) Thick airfoil rotation sensitivity

Figure 1.16: Airfoil displacement and rotation sensitivity results due to change in camber.

As shown in Figure 5.16, the sensitivity response flows the same pattern as the analysis solution for this problem. For the oscillatory response of the thin airfoil, the sensitivity solution also moves between two extremes for both the displacement and airfoil rotation. However, for the thick airfoil that shows a divergence characteristic as shown in Figure 5.14, the sensitivities also reach a constant value. It is interesting to see that for the thick airfoil, by increasing the thickness the lift will increase, and therefore we see positive sensitivities for the displacement; however, the moment generated around the quarter chord decreases which cause a negative sensitivity for the rotation.

Finally, we looked at the u-velocity sensitivity contours as shown in Figure 5.17 for different snapshots in time. As shown here, the velocity field around the airfoil in both cases as the most sensitivity near the tip.

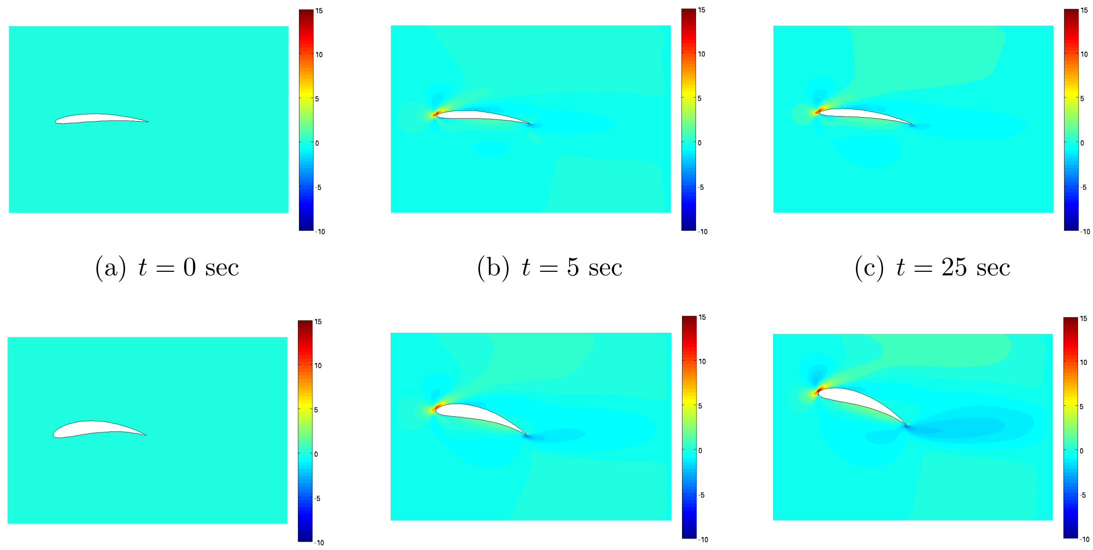

(a) $t = 0$ sec (b) $t = 5$ sec (c) $t = 25$ sec

(d) $t = 0$ sec (e) $t = 5$ sec (f) $t = 25$ sec

Figure 1.17: U-velocity sensitivity time snapeshots for airfoil on elastic structure.

Bibliography

[1] Jendrzejczyk, J. and Chen, S., "Fluid forces on two circular cylinders in crossflow," Tech. rep., Argonne National Lab., 1985.

[2] Sridhar, B., Ng, H., and Chen, N., "Aircraft trajectory optimization and contrails avoidance in the presence of winds," *Journal of Guidance, Control, and Dynamics*, Vol. 34, No. 5, 2011, pp. 1577–1584.

[3] Han, Z.-H., Görtz, S., and Zimmermann, R., "Improving variable-fidelity surrogate modeling via gradient-enhanced kriging and a generalized hybrid bridge function," *Aerospace Science and Technology*, Vol. 25, No. 1, 2013, pp. 177–189.

[4] Pettit, C. L., "Uncertainty quantification in aeroelasticity: recent results and research challenges," *Journal of Aircraft*, Vol. 41, No. 5, 2004, pp. 1217–1229.

[5] Sobieszczanski-Sobieski, J. and Haftka, R. T., "Multidisciplinary aerospace design optimization: survey of recent developments," *Structural optimization*, Vol. 14, No. 1, 1997, pp. 1–23.

[6] Martins, J. R., Sturdza, P., and Alonso, J. J., "The complex-step derivative approximation," *ACM Transactions on Mathematical Software (TOMS)*, Vol. 29, No. 3, 2003, pp. 245–262.

[7] Naumann, U., *The art of differentiating computer programs: an introduction to algorithmic differentiation*, Vol. 24, Siam, 2012.

[8] Choi, K. K. and Kim, N.-H., *Structural sensitivity analysis and optimization 1: linear systems*, Springer Science & Business Media, 2006.

[9] Vanderplaats, G., *Numerical optimization techniques for engineering design: with applications*, McGraw-Hill Series in Mechanical Engineering, McGraw-Hill Ryerson, Limited, 1984.

[10] Arora, J. S. and Haug, E. J., "Methods of design sensitivity analysis in structural optimization," *AIAA journal*, Vol. 17, No. 9, 1979, pp. 970–974.

[11] Reuther, J. J., Jameson, A., Alonso, J. J., Rimllnger, M. J., and Saunders, D., "Constrained multipoint aerodynamic shape optimization using an adjoint formulation and parallel computers, part 2," *Journal of aircraft*, Vol. 36, No. 1, 1999, pp. 61–74.

[12] Martins, J. R., Alonso, J. J., and Reuther, J. J., "A coupled-adjoint sensitivity analysis method for high-fidelity aero-structural design," *Optimization and Engineering*, Vol. 6, No. 1, 2005, pp. 33–62.

[13] Newman, J. C., Taylor, A. C., and Barnwell, R. W., *Aerodynamic shape sensitivity analysis and design optimization of complex configurations using unstructured grids*, National Aeronautics and Space Administration, 1997.

[14] Morris, A., Allen, C., and Rendall, T., "CFD-based optimization of aerofoils using radial basis functions for domain element parameterization and mesh deformation," *International journal for numerical methods in fluids*, Vol. 58, No. 8, 2008, pp. 827–860.

[15] Jameson, A., Shankaran, S., Martinelli, L., and Haimes, B., "Aerodynamic Shape Optimization of Complete Aircraft Configurations using Unstructured Grids," *42nd AIAA Aerospace Sciences Meeting and Exhibit*, AIAA 2004-533, 2004.

[16] Gamboa, P., Vale, J., P. Lau, F., and Suleman, A., "Optimization of a morphing wing based on coupled aerodynamic and structural constraints," *AIAA journal*, Vol. 47, No. 9, 2009, pp. 2087–2104.

[17] Pandya, M. J. and Baysal, O., "Gradient-based aerodynamic shape optimization using alternating direction implicit method," *Journal of aircraft*, Vol. 34, No. 3, 1997, pp. 346–352.

[18] Kim, H.-J., Sasaki, D., Obayashi, S., and Nakahashi, K., "Aerodynamic optimization of supersonic transport wing using unstructured adjoint method," *AIAA journal*, Vol. 39, No. 6, 2001, pp. 1011–1020.

[19] Lyu, Z. and Martins, J. R., "Aerodynamic design optimization studies of a blended-wing-body aircraft," *Journal of Aircraft*, Vol. 51, No. 5, 2014, pp. 1604–1617.

[20] Haftka, R. T. and Adelman, H. M., "Recent developments in structural sensitivity analysis," *Structural optimization*, Vol. 1, No. 3, 1989, pp. 137–151.

[21] Borggaard, J. and Burns, J., "A PDE sensitivity equation method for optimal aerodynamic design," *Journal of Computational Physics*, Vol. 136, No. 2, 1997, pp. 366–384.

[22] Hristova, H., Etienne, S., Pelletier, D., and Borggaard, J., "A continuous sensitivity equation method for time-dependent incompressible laminar flows," *International Journal for numerical methods in fluids*, Vol. 50, No. 7, 2006, pp. 817–844.

[23] Cross, D. M. and Canfield, R. A., "Local continuum shape sensitivity with spatial gradient reconstruction," *Structural and Multidisciplinary Optimization*, Vol. 50, No. 6, 2014, pp. 975–1000.

[24] Arora, J. and Haug, E., "Methods of Design Sensitivity Analysis in Structural Optimization," *AIAA Journal*, Vol. 17, No. 9, 1979, pp. 970–974.

[25] Dems, K. and Mroz, Z., "Variational approach to first- and second-order sensitivity analysis of elastic structures," *International Journal for Numerical Methods in Engineering*, Vol. 21, No. 4, 1985, pp. 637–661.

[26] Borggaard, J. and Burns, J., *A sensitivity equation approach to shape optimization in fluid flows*, Springer, 1995.

[27] Stanley, L. G. D. and Stewart, D. L., *Design Sensitivity Analysis: Computational Issues of Sensitivity Equation Methods*, Frontiers in applied mathematics, Society for Industrial and Applied Mathematics (SIAM, 3600 Market Street, Floor 6, Philadelphia, PA 19104), 2002.

[28] Etienne, S. and Pelletier, D., "A general approach to sensitivity analysis of fluid–structure interactions," *Journal of Fluids and Structures*, Vol. 21, No. 2, 2005, pp. 169–186.

[29] Liu, S. and Canfield, R. A., "Equivalence of continuum and discrete analytic sensitivity methods for nonlinear differential equations," *Structural and Multidisciplinary Optimization*, Vol. 48, No. 6, 2013, pp. 1173–1188.

[30] Sahin, M. and Mohseni, K., "An arbitrary Lagrangian–Eulerian formulation for the numerical simulation of flow patterns generated by the hydromedusa Aequorea victoria," *Journal of Computational Physics*, Vol. 228, No. 12, 2009, pp. 4588–4605.

[31] Liu, S. and Canfield, R. A., "Boundary velocity method for continuum shape sensitivity of nonlinear fluidstructure interaction problems," *Journal of Fluids and Structures*, Vol. 40, No. 0, 2013, pp. 284 – 301.

[32] Peskin, C. S., "Numerical analysis of blood flow in the heart," *Journal of computational physics*, Vol. 25, No. 3, 1977, pp. 220–252.

[33] Anderson, J. D. and Wendt, J., *Computational fluid dynamics*, Vol. 206, Springer, 1995.

[34] Saiki, E. and Biringen, S., "Numerical simulation of a cylinder in uniform flow: application of a virtual boundary method," *Journal of Computational Physics*, Vol. 123, No. 2, 1996, pp. 450–465.

[35] Zhu, L. and Peskin, C. S., "Interaction of two flapping filaments in a flowing soap film," *Physics of Fluids (1994-present)*, Vol. 15, No. 7, 2003, pp. 1954–1960.

[36] Beyer, R. P. and LeVeque, R. J., "Analysis of a one-dimensional model for the immersed boundary method," *SIAM Journal on Numerical Analysis*, Vol. 29, No. 2, 1992, pp. 332–364.

[37] Peskin, C. S. and McQueen, D. M., "A three-dimensional computational method for blood flow in the heart I. Immersed elastic fibers in a viscous incompressible fluid," *Journal of Computational Physics*, Vol. 81, No. 2, 1989, pp. 372–405.

[38] Fauci, L. J. and Peskin, C. S., "A computational model of aquatic animal locomotion," *Journal of Computational Physics*, Vol. 77, No. 1, 1988, pp. 85–108.

[39] Kempe, T., Lennartz, M., Schwarz, S., and Fröhlich, J., "Imposing the free-slip condition with a continuous forcing immersed boundary method," *Journal of Computational Physics*, Vol. 282, 2015, pp. 183–209.

[40] Uhlmann, M., "An immersed boundary method with direct forcing for the simulation of particulate flows," *Journal of Computational Physics*, Vol. 209, No. 2, 2005, pp. 448–476.

[41] Mittal, R. and Iaccarino, G., "Immersed boundary methods," *Annu. Rev. Fluid Mech.*, Vol. 37, 2005, pp. 239–261.

[42] Goldstein, D., Handler, R., and Sirovich, L., "Modeling a no-slip flow boundary with an external force field," *Journal of Computational Physics*, Vol. 105, No. 2, 1993, pp. 354–366.

[43] Durlofsky, L. and Brady, J., "Analysis of the Brinkman equation as a model for flow in porous media," *Physics of Fluids*, Vol. 30, No. 11, 1987, pp. 3329–3341.

[44] Arquis, E. and Caltagirone, J., "Sur les conditions hydrodynamiques au voisinage dune interface milieu fluide-milieu poreux: applicationa la convection naturelle," *CR Acad. Sci. Paris II*, Vol. 299, 1984, pp. 1–4.

[45] Angot, P., "Analysis of singular perturbations on the Brinkman problem for fictitious domain models of viscous flows," *Mathematical methods in the applied sciences*, Vol. 22, No. 16, 1999, pp. 1395–1412.

[46] Gazzola, M., Chatelain, P., Van Rees, W. M., and Koumoutsakos, P., "Simulations of single and multiple swimmers with non-divergence free deforming geometries," *Journal of Computational Physics*, Vol. 230, No. 19, 2011, pp. 7093–7114.

[47] Kevlahan, N. K.-R. and Ghidaglia, J.-M., "Computation of turbulent flow past an array of cylinders using a spectral method with Brinkman penalization," *European Journal of Mechanics-B/Fluids*, Vol. 20, No. 3, 2001, pp. 333–350.

[48] Mohd-Yusof, J., "Combined immersed-boundary/B-spline methods for simulations of ow in complex geometries," *Annual Research Briefs. NASA Ames Research Center= Stanford University Center of Turbulence Research: Stanford*, 1997, pp. 317–327.

[49] Verzicco, R., Mohd-Yusof, J., Orlandi, P., and Haworth, D., "LES in complex geometries using boundary body forces," *Center for Turbulence Research Proceedings of the Summer Program, NASA Ames= Stanford University*, 1998, pp. 171–186.

[50] Verzicco, R., Fatica, M., Iaccarino, G., Moin, P., and Khalighi, B., "Large eddy simulation of a road vehicle with drag-reduction devices," *AIAA journal*, Vol. 40, No. 12, 2002, pp. 2447–2455.

[51] Iaccarino, G. and Verzicco, R., "Immersed boundary technique for turbulent flow simulations," *Applied Mechanics Reviews*, Vol. 56, No. 3, 2003, pp. 331–347.

[52] Clarke, D. K., Hassan, H., and Salas, M., "Euler calculations for multielement airfoils using Cartesian grids," *AIAA journal*, Vol. 24, No. 3, 1986, pp. 353–358.

[53] Kirkpatrick, M., Armfield, S., and Kent, J., "A representation of curved boundaries for the solution of the Navier–Stokes equations on a staggered three-dimensional Cartesian grid," *Journal of Computational Physics*, Vol. 184, No. 1, 2003, pp. 1–36.

[54] Hu, X., Khoo, B., Adams, N. A., and Huang, F., "A conservative interface method for compressible flows," *Journal of Computational Physics*, Vol. 219, No. 2, 2006, pp. 553–578.

[55] Udaykumar, H., Mittal, R., and Shyy, W., "Computation of solid–liquid phase fronts in the sharp interface limit on fixed grids," *Journal of computational physics*, Vol. 153, No. 2, 1999, pp. 535–574.

[56] Borrvall, T. and Petersson, J., "Topology optimization of fluids in Stokes flow," *International journal for numerical methods in fluids*, Vol. 41, No. 1, 2003, pp. 77–107.

[57] Challis, V. J. and Guest, J. K., "Level set topology optimization of fluids in Stokes flow," *International journal for numerical methods in engineering*, Vol. 79, No. 10, 2009, pp. 1284–1308.

[58] Deaton, J. D. and Grandhi, R. V., "A survey of structural and multidisciplinary continuum topology optimization: post 2000," *Structural and Multidisciplinary Optimization*, Vol. 49, No. 1, 2014, pp. 1–38.

[59] LeVeque, R. J. and Li, Z., "Immersed interface methods for Stokes flow with elastic boundaries or surface tension," *SIAM Journal on Scientific Computing*, Vol. 18, No. 3, 1997, pp. 709–735.

[60] Pingen, G., Evgrafov, A., and Maute, K., "Topology optimization of flow domains using the lattice Boltzmann method," *Structural and Multidisciplinary Optimization*, Vol. 34, No. 6, 2007, pp. 507–524.

[61] Gobal, K., Grandhi, R. V., and Kolonay, R. M., "Continuum Sensitivity Analysis for Structural Shape Design Variables Using Finite-Volume Method," *AIAA Journal*, Vol. 53, No. 2, 2014, pp. 347–355.

[62] Mase, G. T., Smelser, R. E., and Mase, G. E., *Continuum mechanics for engineers*, CRC press, 2009.

[63] Haftka, R. T. and Grandhi, R. V., "Structural shape optimizationa survey," *Computer Methods in Applied Mechanics and Engineering*, Vol. 57, No. 1, 1986, pp. 91–106.

[64] Dowding, K. J. and Blackwell, B. F., "Sensitivity analysis for nonlinear heat conduction," *Journal of Heat Transfer*, Vol. 123, No. 1, 2001, pp. 1–10.

[65] Szopa, R., Siedlecki, J., and Wojciechowska, W., "Second order sensitivity analysis of heat conduction problems," *Scientific Research of the Institute of Mathematics and Computer Science*, Vol. 4, No. 1, 2005, pp. 255–263.

[66] Sorli, K. and Skaar, I. M., "Sensitivity Analysis For Thermal Design And Monitoring Problems Of Refractories," Begel House Inc., April 19-24, 2004, Norway.

[67] Szabo, B. A. and Babuška, I., *Finite element analysis*, John Wiley & Sons, 1991.

[68] Wickert, D. P., "Least-squares, continuous sensitivity analysis for nonlinear fluid-structure interaction," Tech. rep., DTIC Document, 2009.

[69] Deaton, J. D. and Grandhi, R. V., "Stiffening of restrained thermal structures via topology optimization," *Structural and Multidisciplinary Optimization*, Vol. 48, No. 4, 2013, pp. 731–745.

[70] Jain, A., Jones, N. P., and Scanlan, R. H., "Coupled flutter and buffeting analysis of long-span bridges," *Journal of Structural Engineering*, 1996.

[71] Arrigan, J., Pakrashi, V., Basu, B., and Nagarajaiah, S., "Control of flapwise vibrations in wind turbine blades using semi-active tuned mass dampers," *Structural Control and Health Monitoring*, Vol. 18, No. 8, 2011, pp. 840–851.

[72] Farhat, C., Van der Zee, K. G., and Geuzaine, P., "Provably second-order time-accurate loosely-coupled solution algorithms for transient nonlinear computational aeroelasticity," *Computer methods in applied mechanics and engineering*, Vol. 195, No. 17, 2006, pp. 1973–2001.

[73] Sotiropoulos, F. and Borazjani, I., "A review of state-of-the-art numerical methods for simulating flow through mechanical heart valves," *Medical & biological engineering & computing*, Vol. 47, No. 3, 2009, pp. 245–256.

[74] Kern, S. and Koumoutsakos, P., "Simulations of optimized anguilliform swimming," *Journal of Experimental Biology*, Vol. 209, No. 24, 2006, pp. 4841–4857.

[75] Lomtev, I., Kirby, R., and Karniadakis, G., "A discontinuous Galerkin ALE method for compressible viscous flows in moving domains," *Journal of Computational Physics*, Vol. 155, No. 1, 1999, pp. 128–159.

[76] Farhat, C., "CFD-based nonlinear computational aeroelasticity," *Encyclopedia of computational mechanics*, Vol. 3, 2004, pp. 459–480.

[77] Cheng, Y., Oertel, H., and Schenkel, T., "Fluid-structure coupled CFD simulation of the left ventricular flow during filling phase," *Annals of biomedical engineering*, Vol. 33, No. 5, 2005, pp. 567–576.

[78] Majumdar, S., Iaccarino, G., and Durbin, P., "RANS solvers with adaptive structured boundary non-conforming grids," *Annual Research Briefs, Center for Turbulence Research, Stanford University*, 2001, pp. 353–466.

[79] Peskin, C. S., "Flow patterns around heart valves: a numerical method," *Journal of computational physics*, Vol. 10, No. 2, 1972, pp. 252–271.

[80] Lee, C., "Stability characteristics of the virtual boundary method in three-dimensional applications," *Journal of Computational Physics*, Vol. 184, No. 2, 2003, pp. 559–591.

[81] Shin, S. J., Huang, W.-X., and Sung, H. J., "Assessment of regularized delta functions and feedback forcing schemes for an immersed boundary method," *International Journal for Numerical Methods in Fluids*, Vol. 58, No. 3, 2008, pp. 263–286.

[82] Roma, A. M., Peskin, C. S., and Berger, M. J., "An adaptive version of the immersed boundary method," *Journal of computational physics*, Vol. 153, No. 2, 1999, pp. 509–534.

[83] Peskin, C. S., "The immersed boundary method," *Acta numerica*, Vol. 11, 2002, pp. 479–517.

[84] Kreissl, S., Pingen, G., and Maute, K., "An explicit level set approach for generalized shape optimization of fluids with the lattice Boltzmann method," *International Journal for Numerical Methods in Fluids*, Vol. 65, No. 5, 2011, pp. 496–519.

[85] Wang, L. and Grandhi, R. V., "Improved two-point function approximations for design optimization," *AIAA journal*, Vol. 33, No. 9, 1995, pp. 1720–1727.

[86] Kamaraju, V. and Narasimham, R., *Linear Systems: Analysis And Applications, Second Edition*, I.K. International Publishing House Pvt. Limited, 2009.

[87] Michler, C., Hulshoff, S., Van Brummelen, E., and De Borst, R., "A monolithic approach to fluid–structure interaction," *Computers & fluids*, Vol. 33, No. 5, 2004, pp. 839–848.

[88] Hu, H. H., Patankar, N. A., and Zhu, M., "Direct numerical simulations of fluid–solid systems using the arbitrary Lagrangian–Eulerian technique," *Journal of Computational Physics*, Vol. 169, No. 2, 2001, pp. 427–462.

[89] Van Loon, R., Anderson, P., Van de Vosse, F., and Sherwin, S., "Comparison of various fluid–structure interaction methods for deformable bodies," *Computers & structures*, Vol. 85, No. 11, 2007, pp. 833–843.

[90] Williamson, C. and Govardhan, R., "Vortex-induced vibrations," *Annu. Rev. Fluid Mech.*, Vol. 36, 2004, pp. 413–455.

[91] Chen, S.-S., *Flow-induced vibration of circular cylindrical structures*, Vol. 414, Hemisphere publishing corporation Washington, DC, 1987.

[92] Mittal, S. and Raghuvanshi, A., "Control of vortex shedding behind circular cylinder for flows at low Reynolds numbers," *International journal for numerical methods in fluids*, Vol. 35, No. 4, 2001, pp. 421–447.

[93] Tuncer, I. H., Walz, R., and Platzer, M. F., "A computational study on the dynamic stall of a flapping airfoil," *AIAA paper*, Vol. 2519, 1998, pp. 1998.

[94] Shyy, W., Lian, Y., Tang, J., Liu, H., Trizila, P., Stanford, B., Bernal, L., Cesnik, C., Friedmann, P., and Ifju, P., "Computational aerodynamics of low Reynolds number plunging, pitching and flexible wings for MAV applications," *Acta Mechanica Sinica*, Vol. 24, No. 4, 2008, pp. 351–373.

[95] Tuncer, I. H. and Platzer, M. F., "Computational study of flapping airfoil aerodynamics," *Journal of Aircraft*, Vol. 37, No. 3, 2000, pp. 514–520.

[96] Lian, Y., Ol, M. V., and Shyy, W., "Comparative study of pitch-plunge airfoil aerodynamics at transitional reynolds number," *AIAA paper*, Vol. 652, No. 2008, 2008, pp. 16.

[97] Webb, C., Dong, H., and Ol, M., "Effects of unequal pitch and plunge airfoil motion frequency on aerodynamic response," *46th AIAA Aerospace Sciences Meeting and Exhibit*, 2008, pp. 7–10.

,